## PAPER

# Nanosized graphene crystallite induced strong magnetism in pure carbon films†

Chao Wang, Xi Zhang and Dongfeng Diao*

We report strong magnetism in pure carbon films grown by electron irradiation assisted physical vapor deposition in electron cyclotron resonance plasma. The development of graphene nanocrystallites in the amorphous film matrix, and the dependence of the magnetic behavior on amorphous, nanocrystallite and graphite-like structures were investigated. Results were that the amorphous structure shows weak paramagnetism, graphene nanocrystallites lead to strong magnetization, and graphite-like structures corresponded with a lower magnetization. At a room temperature of 300 K, the highest saturation magnetization of 0.37 emu $g^{-1}$ was found in the nanosized graphene nanocrystallite structure. The origin of strong magnetism in nanocrystallites was ascribed to the spin magnetic moment at the graphene layer edges.

## 1. Introduction

Carbon based nano devices have bright prospects in the modern semiconductor industry since they can be easily integrated with silicon substrate during fabrication, and they can effectively reduce resource and energy consumptions. Nano devices derived from carbon materials such as graphene[1] and carbon nanotubes[2] have shown significant performances. Recently, nanocrystallite-containing carbon films attracted much attention owing to their unique mechanical,[3] optical,[4] electrical[5] and other properties. They can also be expected as candidates for novel carbon based nano devices.

Other than the mentioned properties, magnetism in pure carbon materials[6–11] has stimulated extensive studies to search for novel metal-free magnetic devices. Magnetic behaviors have been found in various carbon allotropes such as $C_{60}$,[6] carbon nanofoam,[7] nanofibers,[8] irradiated graphite[9,10] and nanodiamond.[11] The prediction of magnetism derived from graphene[12] is particularly intriguing, since graphene is considered as the basis for next generation electronic and spintronics devices.[13] Research on magnetism originating in graphene oxide,[14] graphene nanoflakes,[15,16] hydrogenated graphene[17] and graphene nanoribbons[18] suggested that the magnetic behavior of graphene based materials is in a large part governed by their edge structures. Even in carbon–nitrogen compounds, the magnetism also originates from unpaired carbon atoms at edge defects.[19] Although the mechanism of carbon magnetism is complicated and can be divergent due to different atomic configurations,[20–24] theoretical research has demonstrated that an orderly arrangement of spin magnetic moment at the graphene layer edge is an important source for carbon magnetism, which can be in various types.[25,26] However, the existing approaches for magnetic carbon films need an extra step of treatment to induce magnetism, and the one-step preparation methods only can produce dispersed particles or flakes; the direct growth of strong-magnetic carbon films in a productive manner is still a challenge. Recently discovered magnetism in graphene layer embedded carbon films[27] showed that higher magnetization can be expected if the content of graphene nanocrystallites further increased. Since low energy electron irradiation in plasma-assisting deposition has been found capable to modulate the nanocrystallite formation,[28,29] it is an effective way to modify the magnetic behaviors of pure carbon films by controlling film structures.

In this study, we used low energy electron irradiation in electron cyclotron resonance (ECR) plasma to induce graphene nanocrystallite formation and development in carbon films, thus modulating the film magnetic behaviors. Different electron irradiation densities and energies were employed by altering gas pressure and substrate bias voltage, respectively. The film structures and graphene layer edge development were characterized by transmission electron microscopy (TEM) observation together with Raman spectra analysis. The saturation magnetization, temperature-dependence of magnetization, and electric resistivity of the films were measured. The features and origins of magnetism in different film structures

*Institute of Nanosurface Science and Engineering, Shenzhen University, Shenzhen 518060, China. E-mail: dfdiao@szu.edu.cn; Fax: +86 0755 26902415; Tel: +86 0755 26902415*

were recognized by temperature-dependence measurement of magnetization.

## 2. Experimental details

Film deposition was carried out in an ECR plasma sputtering system, in which the low energy electron irradiation technique was introduced in argon plasma. The realization of electron irradiation is introduced in Fig. S1 in the ESI.†[30] The carbon films were grown on a silicon (100) surface, and the substrate size was $20 \times 20 \times 0.5$ mm$^3$. Before film deposition, the silicon wafer was cleaned in acetone and ethanol bath successively by ultrasonic waves, then was fixed onto the substrate holder and put into the vacuum chamber. The vacuum chamber was pumped down to a base vacuum of $3 \times 10^{-4}$ Pa, then argon gas was inflated to generate plasma. When the plasma was stabilized, the substrate surface was firstly cleaned by argon ions at the bias voltage of $-50$ V for 3 minutes. Thereafter, a sputtering bias voltage of $-300$ V was applied onto the carbon target to generate carbon atoms for film growth. During film growth, low electron irradiation was introduced in order to induce graphene layer growth. In this study, the electron irradiation density varied from $10^{10}$ cm$^{-3}$ to $1.5 \times 10^{11}$ cm$^{-3}$, and the irradiation energy varied from 0 eV to 300 eV. The depositing time was 15 min and the substrate temperature rose from room temperature to less than 200 °C during the deposition process, which was measured using a thermometer.

The structures of carbon films were observed using a JEOL-2010 TEM with the electron acceleration voltage of 200 kV. Plan view TEM specimens were prepared by scraping the film from the Si substrate and transferring the flakes onto a copper micro grid. The bonding structures of the films were studied from their Raman spectra, which were obtained with a HORIBA HR800 laser confocal Raman spectrometer. The 514 nm laser spot size was 2 µm using a 100× objective, and the laser power was kept at 0.1 mW to avoid sample surface heating. The electric resistivity of the films was measured using the four-probe-method, and the saturation magnetizations were obtained from a Superconductivity Quantum Interference Device (SQUID) at a constant temperature of 300 K with the magnetic field intensity between ±10 kOe. Field cooling (FC) and zero field cooling (ZFC) tests were carried out from 3 to 370 K under a magnetic field of 500 Oe.

## 3. Results and discussion

With electron irradiation energies varied from 10 to 300 eV, the carbon films showed different structures as exhibited in Fig. 1, where Raman spectra, electric resistivities and TEM images are listed in (a) to (d). With the irradiation energy of 10 eV, the Raman spectrum showed a broad band from 1100 cm$^{-1}$ to 1800 cm$^{-1}$, with no 2D band detected (labeled as A in blue color), both features indicating an amorphous structure, as shown in Fig. 1(a). When the irradiation energy was

between 40 and 300 eV, the Raman spectra contained separable D and G bands around 1340 cm$^{-1}$ to 1580 cm$^{-1}$. The clear-shaped D band representing the long range ordered structure with sp$^2$ hybridization in amorphous structure. The 2D band also appears in these spectra, suggesting the existence of graphene layers since it arises from the two-phonon involved double resonance Raman process, which typically occurs inside a graphene layer.[31] The increase of 2D band intensity from 40 to 150 eV is another proof for the increasing amount of graphene layers in the films. We refer to the structure with the above Raman features as a nanocrystallite structure, and the films with irradiation energies of 50 and 150 eV were labeled as sample B (red) and C (violet), respectively. When the irradiation energy further increased from 200 eV to 300 eV, the 2D band gradually reduced, which was attributed to the formation of graphite-like structure in the film, where edge defects were less than in the former nanocrystallite containing structure. The film with the irradiation energy of 200 eV was labeled as D (green). The D/G band ratio $I_D/I_G$ for each spectrum was obtained by Breit–Wigner–Fano (BWF) fitting,[32] and the results are shown in Fig. 1(c), together with the film resistivity. It is clear that from the amorphous (A) to nanocrystallite structure (B) the $I_D/I_G$ value showed a steep increment from 0.4 to 1.2, which further confirmed the formation of nanocrystallites.[33] The film electric resistivity suddenly dropped by one order of magnitude due to the formation of graphene nanocrystallites, which were more conductive than the amorphous structure. The structural change from nanocrystallite (C) to graphite-like (D) can be seen from the reduction of both the $I_D/I_G$ ratio and electric resistivity, and barely changed for irradiation energies higher than 200 eV, since the structure remained graphite-like in those cases.

In our research, the 2D band shape evolved with different film structures, and the change can be clearly described by Lorentz fitting results, as shown in Fig. 1(b). For amorphous structure (A), no 2D band was detected. For the graphene nanocrystallite structure (from B to C), the 2D bands are precisely fitted with four Lorentz components, representing an electronic structure similar to bilayer graphene.[28,34,35] For the graphite-like structure, more than four components are needed to fit the 2D band, because more peaks appeared at the band shoulders, indicating a more complicated electronic structure than bilayer graphene due to the merging of graphene layer edges between nanocrystallites. This feature of the 2D band can be helpful in our study to identify whether the film has a nanocrystallite structure or graphite-like structure.

Different film structures can be seen in the TEM images in Fig. 1(d). For sample A, the TEM image showed an amorphous structure, with no graphene layers observed in the film. For sample B, small sized graphene nanocrystallites can be seen, each containing several graphene layers, and the graphene layer showed twisting and curving. For sample C, more graphene nanocrystallites were found, while no obvious difference from sample B was seen. For sample D, instead of small sized nanocrystallites, a bulk graphite-like structure with orderly aligned graphene layers can be seen. The lateral sizes of the
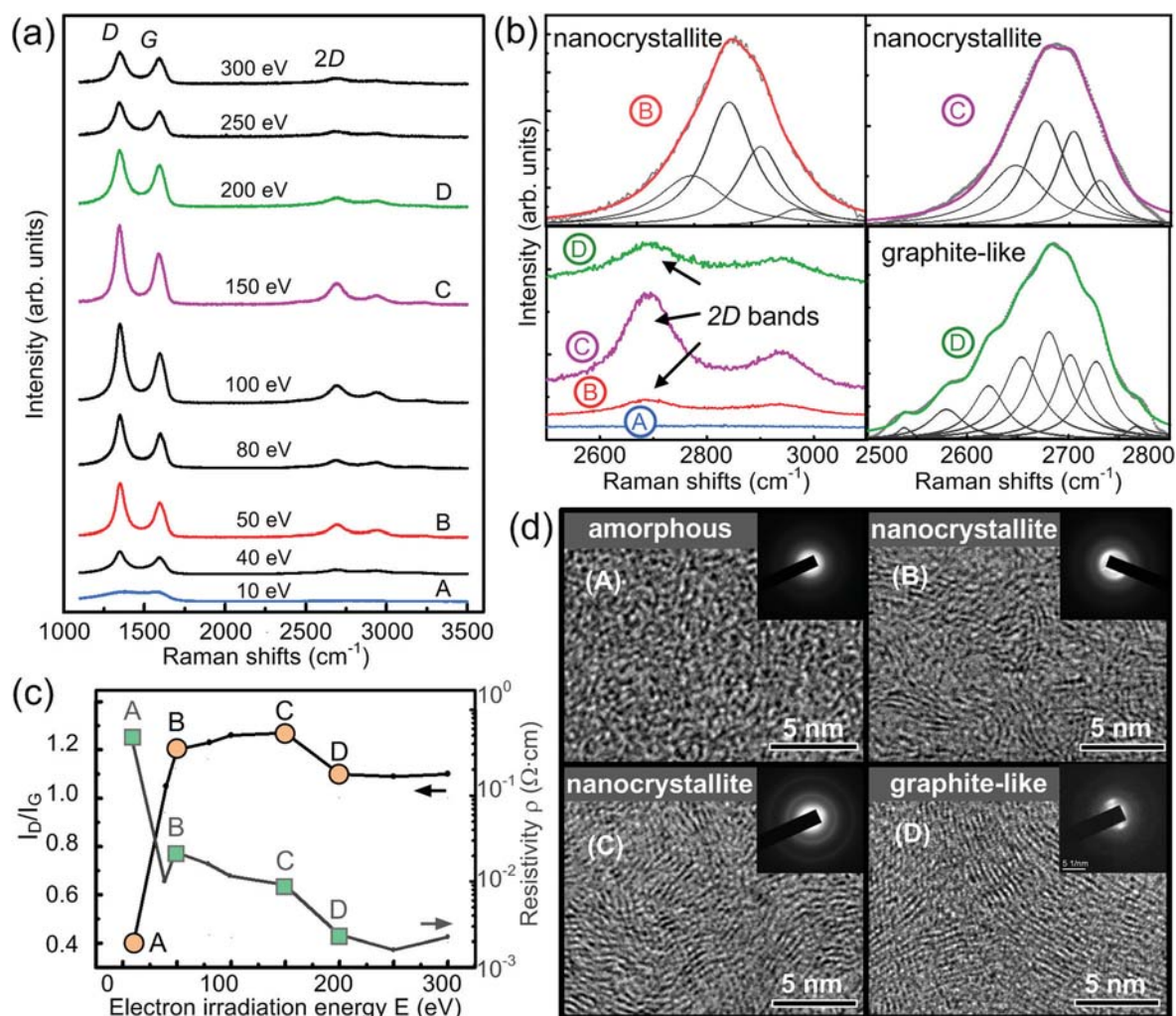
Fig. 1 (a) Raman spectra of carbon films with different electron irradiation energies from 10 to 300 eV under the irradiation density of $10^{11}$ cm$^{-3}$. The spectra at 10, 50, 150 and 200 eV were labeled as A (blue), B (red), C (violet) and D (green), revealing the films of different structures. (b) Detailed spectra between 2500 cm$^{-1}$ and 2800 cm$^{-1}$, where 2D bands of samples B, C and D were pointed out. (c) The D band and G band ratios obtained from the Raman spectra of the films as well as their electrical resistivities. (d) Plan-view TEM images of samples A–D and their electron diffraction patterns.

graphene layers became larger, and the graphene layer stacks connected with each other, which led to less graphene layer edges between stacks. Due to our TEM observation, the nanocrystallites and graphene layers existed not only in the area shown in the figure, but also in the whole film. From the above results, we can see that the TEM images and Raman spectra keep good agreement in telling the differences between amorphous, nanocrystallite and graphite like structures. When the irradiation energy was between 50 and 150 eV, graphene layer edges gradually increased due to the increase of small sized few layer graphene stacks, and with the irradiation energy larger than 200 eV, the film structures were still graphite-like, which can be seen from TEM images in Fig. S2.†[30]

The magnetic behaviors of the films were measured with a SQUID MPMS-XL-7 from Quantum Design at the constant temperature of 300 K, which is the most probable temperature

in a real application atmosphere. During measurement, the effect of magnetic contamination was negligible according to plasma mass spectrometry tests on the impurity element concentrations.†[30] For each measurement, the magnetic field was applied from 0 to +10 kOe, then changed from +10 kOe to −10 kOe, and finally went back to 0, hence a hysteresis loop was obtained. Different changing rates of magnetic field were employed, which increased from 0.02 (−0.1 to +0.1 kOe) to 0.5 (±3 to ±10 kOe). This data acquisition method was used in order to shorten the measuring process and detailed information also can be seen at the lower magnetic field range. The magnetization curves (M–H curves) of samples A–D are shown in Fig. 2(a), where different saturation magnetizations $M_s$ can be seen. For the amorphous structure with no graphene layer edges (sample A), $M_s$ was 0.017 emu g$^{-1}$. When graphene layer edges were formed (sample B), $M_s$ increased to 0.075 emu g$^{-1}$. When more graphene nanocrystallites were produced in the
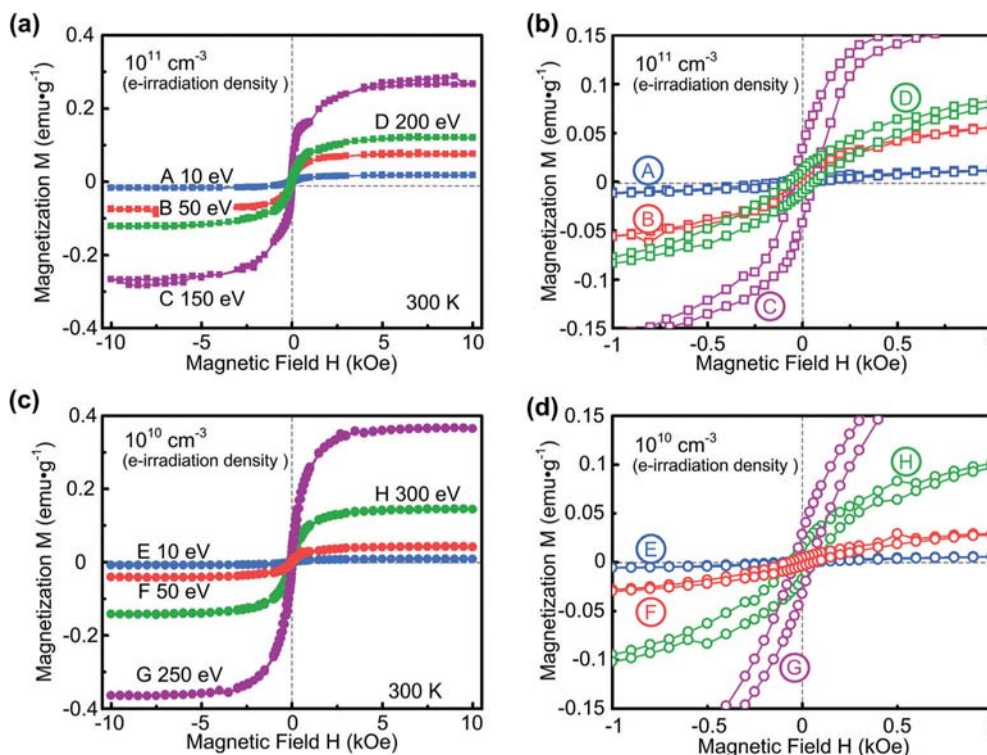
**Fig. 2** Magnetization curves of carbon films with different structures at the temperature of 300 K. Diamagnetic signals from plastic foils and capsules have been subtracted. The magnetization results for samples A–D are plotted in (a) with solid squares. The hysteresis loops in a smaller magnetic field region are plotted in (b) with hollow squares. When the electron irradiation density was reduced by an order of magnitude, films with different structures were obtained, which are listed as samples E–H. The magnetization results for samples E–H are plotted in (c) with solid circles, and the hysteresis loops are plotted in (d) with hollow circles.

film (sample C), $M_s$ further increased to 0.27 emu g$^{-1}$. When graphite-like structure was formed (sample D), $M_s$ decreased to 0.12 emu g$^{-1}$. Fig. 2(b) presents the hysteresis loops in a smaller magnetic field region, in which the change in residual magnetism $B_r$ can be seen more clearly (detailed values are plotted in Table S2†[30]). Like the saturation magnetization, the $B_r$ value increased when the amorphous structure (A) changed into the nanocrystallite structure (B), and reached a maximum (C) before the film structure further changed into graphite-like (D).

A similar relationship between magnetization and the development of film structure was also noticed when film growth was carrying out under an electron irradiation density of 10$^{10}$ cm$^{-3}$. The magnetic measurement results are shown in Fig. 2(c), where the increasing of $M_s$ can be clearly seen with the increasing of graphene nanocrystallites. An amorphous structure was obtained at the irradiation energy of 10 eV (sample E), and the magnetization was 0.008 emu g$^{-1}$. Small sized nanocrystallites appeared at the energy of 50 eV (sample F), and the magnetization rose to 0.04 emu g$^{-1}$. The film magnetization reached a maximum of 0.37 emu g$^{-1}$ at 250 eV (sample G), larger than the recently reported room temperature magnetization in pure-carbon allotropes.[14–17,36,37] When the structure changed into graphite-like at 300 eV (sample H), the magnetization reduced to 0.14 emu g$^{-1}$. Comparing with Fig. 2(b), the hysteresis loops in Fig. 2(d) also clearly show that

the nanocrystallite structure can possess a larger residual magnetism when grown under lower irradiation density. Although the irradiation energies for achieving maximum $M_s$ are different, it is quite evident that the increase in graphene nanocrystallites can lead to strong magnetism and graphite-like structures are less "magnetic" than graphene nanocrystallite structures.

In order to further recognize the magnetic properties of the films, field cooling (FC) and zero-field cooling (ZFC) measurements were carried out for the amorphous structure (sample E) and nanocrystallite structure (sample G) at 500 Oe, and different types of temperature dependence were found, as shown in Fig. 3. The background diamagnetic signals from plastic foils and capsules have been subtracted. For the amorphous structure, the FC curve (red) and ZFC curve (blue) almost coincided with each other as shown in Fig. 3(a), and exhibited weak paramagnetic behavior. The slight divergence may come from the free spins which are of very low concentration in the amorphous carbon base. On the other hand, a clearer separation can be seen between the FC and ZFC curves for the nanocrystallite structure, in the temperature range of 350 K to 250 K, where the ZFC curve reached its maximum value. The maximum point of the ZFC curve can usually represent the blocking temperature of a magnetic system,[38–41] however, the size of graphene nanocrystallites are not exactly the same, so the blocking temperature may be different since
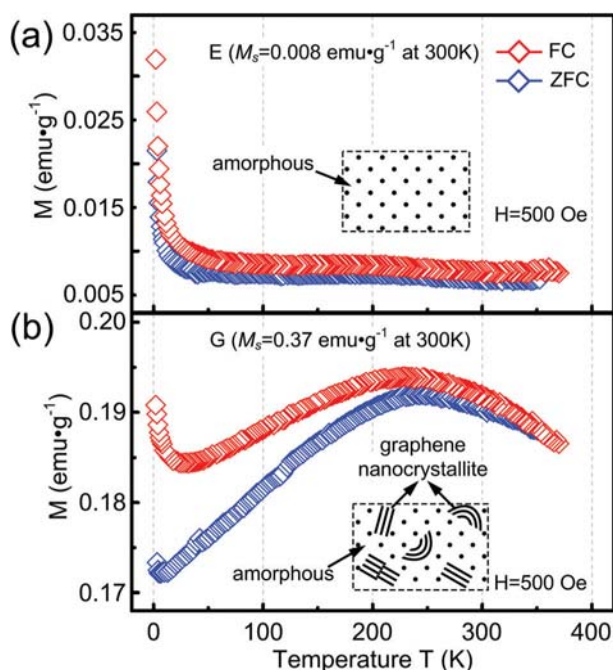
Fig. 3 FC and ZFC curves of (a) amorphous (sample E) and (b) nano-crystallite structure (sample G) under applied magnetic field of 500 Oe. The diamagnetic signals from the background have been subtracted.
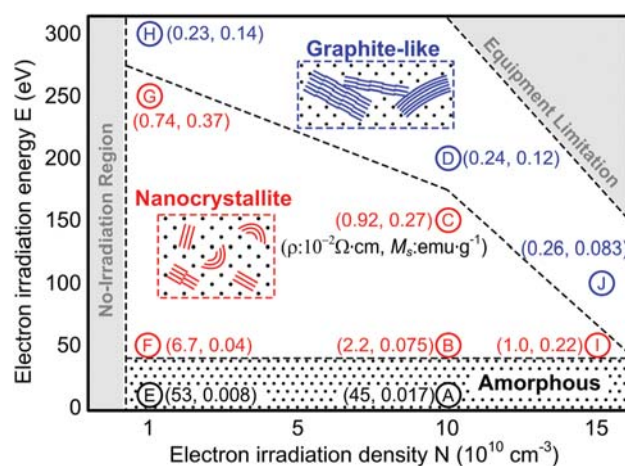


Fig. 4 The structure–magnetization diagram of magnetic carbon films as a function of electron irradiation energy and density. Electric resistivity is labeled in the unit of $\Omega$ cm, followed by saturation magnetization in the unit of emu g$^{-1}$. The grey region in the figure means film could not be obtained so far due to current equipment limitation in our study.

the size of "magnetic particle" can influence the blocking temperature. We think that is why the curves did not clearly show a separation at 250 K where the ZFC curve reached its maximum value. Actually, we tend to believe the vibration of blocking temperature ranges from 250 K to 350 K, where the separation starts. From 250 K to 30 K, the FC curve showed a trend of decreasing magnetization and at low temperature (less than 30 K), the paramagnetic behavior of the amorphous matrix of the film is still detectable.

However, the magnetism originating from nanocrystallites is predominant during most of the measurement. Therefore, the strong carbon magnetism in our study is mainly ascribed to the nanocrystallite structure. Furthermore, we already found that the magnetism will become weaker for graphite-like structures that contain larger graphene layers than the nanocrystallite structure did. Therefore, the strong magnetism is more possibly originated from the graphene layer edges, which are more concentrated in the nanocrystallite structure than in the graphite-like structure, and increases proportionately with the formation of nanocrystallites.

In the aim of revealing the relationship between graphene layer edges and magnetic behaviors, more carbon films were deposited under different electron irradiation densities and energies, with the density range expanded to $10^{10}$–$1.5 \times 10^{11}$ cm$^{-3}$, and energy range 10–350 eV. Electron irradiation with density lower than $10^{10}$ cm$^{-3}$ could not be realized in our study since plasma was not stable under such a low density, and for the irradiation density of $1.5 \times 10^{11}$ cm$^{-3}$, the electron current density will reach the equipment limitation when the irradiation energy was higher than 150 eV. Saturation magneti-

zation values and electric resistivities were measured for each film, and their structures were observed focusing on the nano-crystallite size and formations. The overall results are summarized in Fig. 4 as a structure–magnetization diagram of the magnetic carbon films. The samples near the boundaries between different structures are listed from A to J. The electric resistivity and saturation magnetization of each sample are also labeled in the figure.

The diagram clearly shows that strong magnetization can be obtained in the region where the nanocrystallite structure can be obtained. For the same electron irradiation density, the highest magnetization was achieved when graphene nanocrystallites were mostly yielded before graphite-like structure was formed. The diagram also shows that lower irradiation density was beneficial for stronger magnetism. This is because a higher irradiation energy can be reached with a lower electron irradiation density before graphite-like structure formation, thus leading to a high content of nanocrystallites.

On the other hand, the film electrical resistivity was not determined by graphene layer edges. Instead, it showed a clearly dependence on the graphene layer content. For the same irradiation density, the resistivity value drops by one order of magnitude with the change from amorphous to nano-crystallite structure, and nanocrystallite to graphite-like structure. So it can be inferred that the electric property was governed by the amount and size of graphene layers rather than graphene layer edges.

Fig. 5 summarizes the changing tendencies of resistivity and saturation magnetization along with different film structures. As exhibited in the figure, graphene nanocrystallites can bring about larger magnetization than other structures. The structural evolution from graphene nanocrystallite to graphite-like structure leads to better electric performance but at the same time results in lower magnetization. The figure also suggests that lower electron irradiation density is preferred to
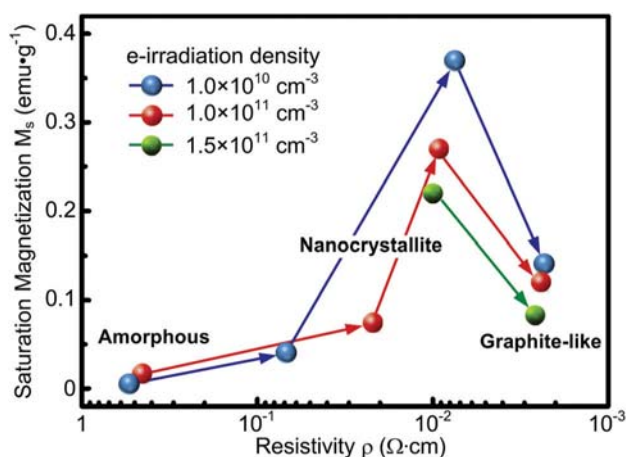
**Fig. 5** Resistivity and magnetization changing tendencies of carbon films along with different film structures.

obtain strong magnetization for the nanocrystallite structure since a larger amount of nanocrystallites are yielded. So for magnetic and spintronics applications, it is necessary to produce more nanosized graphene crystallites, so that graphene layer edges are abundant in the carbon films.

Our related simulation works have confirmed that the under coordinated carbon atoms at graphene layer edges can trap the net spin moment, which leads to strong magnetic behaviors.[42] So the spin at the graphene layer edges may be the origin of the strong magnetic behavior in this research. From TEM and Raman observations, we note that the structural transition of samples A–D and E–H follow the order of: amorphous, nanocrystallite, abundant nanocrystallite and graphite-like. Magnetic measurements revealed that strong magnetism was achieved in samples C and G, which are in the "abundant nanocrystallite" stage, and graphene layer edges are mostly produced at this stage. So we suggest that the origin of the strong magnetism may come from the graphene layer edges.

## 4.   Conclusion

In order to explore strong magnetism in pure carbon films and recognize the role of graphene layer edges in film magnetic behaviors, we performed low energy electron irradiation to modulate graphene nanocrystallite development in film deposition. Pure carbon films with amorphous, nanocrystallite and graphite-like structures were obtained. Magnetization studies showed that by increasing the amount of graphene nanocrystallites, the film magnetization can achieve 0.37 emu g$^{-1}$ from 0.008 emu g$^{-1}$. Hysteresis loops and FC/ZFC measurements confirmed the strong magnetic behavior of the graphene nanocrystallites. The origin of the strong magnetism of the film was derived from the spin magnetic moment at graphene layer edges in nanosized crystallites. A diagram of structure–magnetization evolution was proposed, and the fact was found that

small size nanocrystallites are beneficial for strong magnetization since they provide a large amount of graphene layer edges. This research brings about an effective way to fabricate pure carbon films with strong magnetism, which are candidates for potential applications in spintronics and nanoelectromechanical systems.

## References

1   F. Schwierz, *Nat. Nanotechnol.*, 2010, **5**, 487.
2   T. Yamada, Y. Hayamizu, Y. Yamamoto, Y. Yomogida, A. Izadi-Najafabadi, D. N. Futada, D. N. Futaba and K. Hata, *Nat. Nanotechnol.*, 2011, **27**, 296.
3   D. W. M. Lau, D. G. McCulloch, M. B. Taylor, J. G. Partridge, D. R. McKenzie, N. A. Marks, E. H. T. Teo and B. K. Tay, *Phys. Rev. Lett.*, 2008, **100**, 176101.
4   M. Shakerzaeh, N. Xu, M. Bosman, B. K. Tay, X. Wang, E. H. T. Teo, H. Zheng and H. Yu, *Carbon*, 2011, **49**, 1018.
5   Y.-Z. Chen, H. Medina, H.-C. Lin, H.-W. Tsai, T.-Y. Su and Y.-L. Chueh, *Nanoscale*, 2015, **7**, 1678.
6   T. L. Makarova, B. Sundqvist, R. Hohne, P. Esquinazi, Y. Kopelevich, P. Scharff, V. A. Davydov, L. S. Kashevarova and A. V. Rakhmanina, *Nature*, 2001, **413**, 716.
7   A. V. Rode, E. G. Gamaly, A. G. Christy, J. G. F. Gerald, S. T. Hyde, R. G. Elliman, B. Luther-Davies, A. I. Veinger, J. Androulakis and J. Giapintzakes, *Phys. Rev. B: Condens. Matter*, 2004, **70**, 054407.
8   S. Ma, J. H. Xia, V. V. S. S. Srikanth, X. Sun, T. Staedler, X. Jiang, F. Yang and Z. D. Zhang, *Appl. Phys. Lett.*, 2009, **95**, 263105.
9   P. Esquinazi, D. Spemann, R. Hohne, A. Setzer, K. H. Han and T. Butz, *Phys. Rev. Lett.*, 2003, **91**, 227201.
10   O. V. Yazyev, *Phys. Rev. Lett.*, 2008, **101**, 037203.
11   S. Talapatra, P. G. Ganesan, T. Kim, R. Vajtai, M. Huang, M. Shima, G. Ramanath, D. Srivastava, S. C. Deevi and P. M. Ajayan, *Phys. Rev. Lett.*, 2005, **95**, 097201.
12   Y. W. Son, M. L. Cohen and S. G. Louie, *Nature*, 2006, **444**, 347.
13   O. V. Yazyev and M. L. Katsnelson, *Phys. Rev. Lett.*, 2008, **100**, 047209.
14   Y. Wang, Y. Huang, Y. Song, X. Zhang, Y. Ma, J. Liang and Y. Chen, *Nano Lett.*, 2009, **9**, 220.
15   A. Ney, P. Papakonstantinou, A. Kumar, N. G. Shang and N. Peng, *Appl. Phys. Lett.*, 2011, **99**, 102504.
16   C. S. Rout, A. Kumar, N. Kumar, A. Sundaresan and T. S. Fisher, *Nanoscale*, 2011, **3**, 900.

17 L. Xie, X. Wang, J. Lu, Z. Ni, Z. Luo, H. Mao, R. Wang, Y. Wang, H. Huang, D. Qi, *et al.*, *Appl. Phys. Lett.*, 2011, **98**, 193113.

18 G. Z. Magda, X. Jin, I. Hagymasi, P. Vancso, Z. Osvath, P. Nemes-Incze, C. Hwang, L. P. Biro and L. Tapaszto, *Nature*, 2014, **514**, 608.

19 D. Gao, Q. Xu, J. Zhang, Z. Yang, M. Si, Z. Yan, M. Su, Z. Yan and D. Xue, *Nanoscale*, 2014, **6**, 2577.

20 Y. W. Son, M. L. Cohen and S. G. Louie, *Phys. Rev. Lett.*, 2006, **97**, 216803.

21 H. Santos, A. Ayuela, L. Chico and E. Artacho, *Phys. Rev. B: Condens. Matter*, 2012, **85**, 245430.

22 M. J. Schmidt and D. Loss, *Phys. Rev. B: Condens. Matter*, 2010, **82**, 085422.

23 W. Li, M. Zhao, Y. Xia, R. Zhang and Y. Mu, *J. Mater. Chem.*, 2009, **19**, 9274.

24 R. R. Nair, M. Sepioni, I-L. Tsai, O. Lehtinen, J. Keinonen, A. V. Krasheninnikov, T. Thomson, A. K. Geim and I. V. Grigorieva, *Nat. Phys.*, 2012, **8**, 199.

25 H. Feldner, Z. Y. Meng, T. C. Lang, F. F. Assaad, S. Wessel and A. Honecker, *Phys. Rev. Lett.*, 2011, **106**, 226401.

26 M. Golor, S. Wessel and M. J. Schmidt, *Phys. Rev. Lett.*, 2014, **112**, 046601.

27 C. Wang and D. Diao, *Appl. Phys. Lett.*, 2013, **102**, 052402.

28 C. Wang, D. Diao, X. Fan and C. Chen, *Appl. Phys. Lett.*, 2012, **100**, 231909.

29 C. Wang and D. Diao, *Surf. Coat. Technol.*, 2011, **206**, 1899–1904.

30 See ESI† for detailed description of low energy electron irradiation technique, more TEM images of carbon films deposited under different electron irradiation energies and plasma mass spectrometry test results.

31 L. M. Malard, M. A. Pimenta, G. Dresselhaus and M. S. Dresselhaus, *Phys. Rep.*, 2009, **473**, 51.

32 S. D. M. Brown, A. Jorio, P. Corio, M. S. Dresselhaus, G. Dresselhaus, R. Saito and K. Kneipp, *Phys. Rev. B: Condens. Matter*, 2001, **63**, 155414.

33 A. C. Ferrari and J. Robertson, *Phys. Rev. B: Condens. Matter*, 2000, **61**, 14095.

34 A. C. Ferrari, J. C. Meyer, V. Scardaci, C. Casiraghi, M. Lazzeri, F. Mauri, S. Piscanec, D. Jiang, K. S. Novoselov, S. Roth, *et al.*, *Phys. Rev. Lett.*, 2006, **97**, 187401.

35 M. Okano, R. Matsunaga, K. Matsuda, S. Masubuchi, T. Machida and Y. Kanemitsu, *Appl. Phys. Lett.*, 2011, **99**, 151916.

36 S. Qin, X. Guo, Y. Cao, Z. Ni and Q. Xu, *Carbon*, 2014, **78**, 559.

37 H. S. S. Ramakrishna Matte, K. S. Subrahmanyam and C. N. R. Rao, *J. Phys. Chem. C*, 2009, **113**, 9982.

38 A. Ludwig, L. Agudo, G. Eggeler, L. Ludwig, A. D. Wieck and O. Petracic, *Appl. Phys. Lett.*, 2013, **113**, 043917.

39 J. T. Abiade, S. H. Oh, D. Kumar, M. Varela, S. Pennycook, H. Guo, A. Gupta and J. Sankar, *Appl. Phys. Lett.*, 2008, **104**, 073910.

40 M. Knobel, W. C. Nunes, H. Winnishofer, T. C. R. Rocha, L. M. Socolovsky, C. L. Mayorga and D. Zanchet, *J. Non-Cryst. Solids*, 2007, **353**, 743.

41 H. Mamiya, M. Ohnuma, I. Nakatani and T. Furubayashim, *IEEE Trans. Magn.*, 2005, **41**, 3394.

42 X. Zhang, C. Wang, C. Q. Sun and D. Diao, *Appl. Phys. Lett.*, 2014, **105**, 042402.